In situ and operando observation of surface oxides during oxygen evolution reaction on copper

Cigdem Toparli[a], Adnan Sarfraz[a], Andreas D. Wieck[b], Michael Rohwerder[a], Andreas Erbe[a,c]

[a] *Max-Planck-Institut für Eisenforschung GmbH, Max-Planck-Str. 1, 40237 Düsseldorf, Germany.*
[b] *Chair for Applied Solid State Physics, Ruhr-Universität Bochum, Universitätsstr. 150, 44780 Bochum, Germany.*
[c] *Department of Materials Science and Engineering, NTNU, Norwegian University of Science and Technology, 7491 Trondheim, Norway.*

Abstract

Formation and dissolution of oxide on copper under transpassive conditions, i.e. during OER and transpassive dissolution, in alkaline electrolyte was investigated by a combination of electrochemical techniques and in situ and operando Raman and photoluminescence (PL) spectroscopy, as well as spectropscopic ellipsometry. Experiments were conducted under potentiodynamic and potentiostatic polarisation in 0.1M NaOH. In chronoamperometry experiments with steps between potentials, oxide thickness continued increasing beyond the onset of OER. The thickness dropped significantly from >10 nm to <5 nm ≈400 mV above the OER onset. The presence of CuO, Cu_2O and Cu_4O_3 was observed by Raman spectroscopy after the onset of OER. Correlating with the thickness drop, strong PL was observed at 1.55 eV, indicating the formation of singly charged oxygen vacancies V_O^+, following the classical PL spectrum interpretation from the literature. PL observation speaks against vacancy pair coalescence as mechanism of dissolution. After electrochemical experiments, the films were n-type semiconductors, not p-type conductors as expected for copper oxides. Results indicate that transpassive dissolution may be triggered by the instability of the oxide with respect to defect formation.

Keywords: `Defect formation, Passivity, Transpassivity, Oxygen`

*Corresponding author
Email address: `a.erbe@mpie.de, aerbe@arcor.de` (Andreas Erbe)

evolution reaction, Copper oxides

1. Introduction

Many metals form a passivating oxide layer at potentials above their reversible dissolution potential [1–3]. In many cases, the oxide layers loose their protective properties above a certain potential, when transpassive dissolution occurs, accompanied by the oxygen evolution reaction (OER) if the potential is sufficiently high [1–3]. OER is in general linked to transpassive metal dissolution, which is in turn related to the stability of the surface oxide [4–7]. It is generally accepted that an oxide layer is present on the electrode surface during OER [8–14]. Hence, understanding the properties of the oxide film on the electrode during OER is critical to foster water splitting. In particular, it is relevant to investigate what drives the transition from the passive to the transpassive state, and how the state of the oxide is after this transition.

Three theoretical concepts are dominating the literature discussion to explain the transition from the passive to the transpassive state of an electrode: (i) the bipolar passive film model, (ii) the surface charge approach, and (iii) the point defect model [15–19]. The bipolar passive film model treats the passive film as an ionic flow rectifier which limits ion adsorption and ingress, and prevents localized corrosion [15]. The surface charge approach assumes that the passive film consists of an n-type semiconductor|insulator|p-type semiconductor (n-i-p) structure [17]. According to this model, oxygen vacancies (donors) are formed during the film growth near the metal, while metal vacancies (acceptors) are generated during dissolution at the layer|electrolyte interface. In this model, the accumulation of positive and negative defects brings non-stationary film growth with complex processes including defect formation, uncontrolled film growth and dissolution. In the point defect model, the concentration of both positive and negative defects increases during passivity break down [19]. Moreover, it is proposed that condensation of the mobile cation vacancies at the film / electrolyte interface causes the destruction of the barrier layer. All aforementioned models were deduced from electrochemical methods and mathematical modelling [2]. During OER on certain metals, e.g. Co, Ni and Mn, the presence of metal cations in a high valance state

was proposed [14, 20–22]. These species were proposed to be active species for OER catalysis [14, 21, 22]. For a further understanding of the effect of OER on transpassive dissolution, it is crucial to assess the changes in the oxide film that are occurring during and after the onset of OER. Spectroelectrochemical techniques can be used to probe the interface in situ and operando during the electrochemical treatment.

In situ Raman spectroscopy has been used repeatedly to observe nature, stability of oxides during OER, and indirectly, also metal oxidation state [14, 23–28]. Electrochemistry combined with Raman spectroscopy on Ni-Fe electrocatalysts identified the formation of different oxides and suggested that disordered NiOOH species are the catalytically active species for OER [23]. The presence of Fe in Ni catalysts was also found to increase the redox potential of the reaction of $Ni(OH)_2$ to NiOOH [24]. In situ UV-vis spectroscopy studies of an NiFeB catalyst suggested a darkening of the active catalyst during OER. Moreover, for this catalyst the presence of negatively charged $NiOO^-$ sites has been reported [25]. Formation of γ-NiOOH before the OER has been shown [25, 26]. It was shown via in situ X-ray absorption spectroscopy that mixed Ni-Fe electrocatalysts include Ni(III) species during OER [27]. For Co, in situ Raman studies showed that during OER, first Co_3O_4 formed, which then underwent a transformation to CoO(OH) [28]. Overall, in situ Raman spectroscopy studies suggest that metal cations in a high valance state and hydroxide species are the active species for OER for some specific systems. It remains to be discussed how general these observations are, e.g. on metals which are not usually occurring in high oxidation states. Further, it is necessary to understand the electronic structure of the oxides during running OER.

This work focusses on the structural and electronic properties of copper oxides during the electrochemical water oxidation. Cu was chosen as a model because it is a unique metal with its electron configuration $3d^{10}\ 4s^1$ [29], and because it is one of the few metals whose oxides are predominantely p-type semiconductors [2]. Copper oxides have attracted considerable interest due to their low band gap ranging between 2.1 and 1.4 eV and also as being intrinsic p-type semiconductors [30]. The character of the oxide on a metal in the passive and transpassive state is critical for electron transfer reactions on its surface [2].

The aim of this study is to understand the relation between surface electronic state,

defects, and nature of oxide under conditions of transpassive dissolution and OER in alkaline solution. The stability and oxide growth was investigated via in situ and operando spectroscopic ellipsometry. The structural properties were studied by in situ Raman spectroscopy, while electronic structure of the oxide layer was deduced both from in situ spectroscopic ellipsometry (SE) and photoluminescence (PL) spectroscopy. To connect the results from here to more versatile electron-spectroscopic characterisation methods typically employed in vacuum, optical post mortem ex situ investigations were complemented by X-ray photoelectron spectroscopy (XPS) analysing both photoelectron and Auger peaks. As comparison of ex situ and in situ Raman spectra has already shown significant differences for the copper system [31], the use of ex situ methods has been limited here.

2. Materials and methods

2.1. Sample preparation

Evaporated copper on silicon wafers was used as a working electrode for in situ spectroscopic ellipsometry experiments. Si(100) wafers (Siegert Wafer, Aachen, Germany) were cleaned with neutral detergent (Extran; VWR), rinsed with deionised water and 2-propanol, and finally dried. Firstly, a 10 nm chromium adhesion layer was deposited on the silicon surface by evaporation. Subsequently, copper was deposited by electron beam evaporation. Chromium and copper pellets with purity 99.999% (Wieland Edelmetalle, Pforzheim, Germany) were used. All evaporation was carried out in a Leybold Univex 450 chamber. During evaporation, the pressure was around $6 \cdot 10^{-7}$ mbar. Copper was evaporated at an evaporation rate of 10 nm min^{-1}. Typically, a layer with thickness of 200 nm was obtained.

Polycrystalline Cu foil of 4 mm thickness with a purity of 99.5% (Goodfellow) was used as alternative working electrode for in situ Raman spectroscopy experiments.[1] The samples were mechanically ground with SiC paper up to 4000 grit and subsequently

[1] In some experiments, Cu foil was used rather than evaporated Cu on Si to prevent ambiguities in the spectrum interpretation due to the presence of the extremely strong fundamental Si phonon at 520 cm^{-1}. This peak might appear if significant amounts of copper had been dissolved.

polished with polishing suspensions (3 µm, 1 µm and 100 nm SiO_2, pH = 9) to obtain a smooth surface. Afterwards, the sample was sonicated in ethanol for 5 min and dried in a nitrogen stream.

2.2. In situ spectroscopic ellipsometry (SE)

In situ spectroscopic ellipsometry experiments were performed using an SE 800 spectroscopic ellipsometer (Sentech Instruments, Krailling/Berlin, Germany) working in the wavelength range of 280-810 nm (1.5-4.4 eV). The measurements were carried out during both dynamic potential scan (cyclic voltammetry; CV) and potentiostatic polarisation (chronoamperometry; CA). The electrode potential was controlled by a Compactstat potentiostat (Ivium Technologies, Eindhoven, The Netherlands). The details of the in situ cell were described elsewhere [32, 33].

A freshly prepared Cu sample was directly mounted in the optical-electrochemical cell, which was equipped with liquid flow connections. Cu tape was used to provide the electric contact to the surface of the sample. A Pt mesh counter electrode and an Ag|AgCl|3M KCl microreference electrode (DriRef-2SH, World Precision Instruments, Sarasota, FL, USA) were used to conduct the electrochemical part of the experiment. The electrode potential of the microreference electrode has been determined as +0.208 mV vs. standard hydrogen electrode by a calibrated Ag|AgCl|3M KCl electrode (Metrohm, Filderstadt, Germany). All electrode potentials reported in this work are referenced against Ag|AgCl|3M KCl. 0.1M NaOH was used as electrolyte. The electrolyte was externally purged with argon, and flowed through the cell with a rate of 2 mL min^{-1} using a peristaltic pump (Ismatec IDEX Health and Science, Glattbrugg, Switzerland). During the measurement, the pump rate was reduced to 10.6 µL min^{-1}. In this work, duration of a single ellipsometric measurement was 23.5 s.

Ellipsometric measurements during CV were conducted during scanning the electrode potential at a rate of 2 mV s^{-1} in the potential range of -1.3 V to 0.8 V. An initial potential of 0 V was applied to start the experiments with an initial cathodic scan to -1.3 V. After this reduction of the surface, the sample was oxidised and held at potentials up to 0.8 V. The CA experiments were performed starting from -1.0 V to clean the surface. Subsequently, the surface was oxidised in steps of 0.1 V up to 1.0 V. Each

potential was applied for 100 s, except the initial reduction at -1.0 V, which was applied for 5 min.

Data analysis was conducted as described in detail previously [31, 32]. In brief, an extension of Lekner's first order perturbation approach [34] without using any optical data modelling was used. The first order perturbation parameter J_1 for a substrate-layer-ambient system was defined in terms of dielectric functions, which is related to the complex refractive index $n + Ik$, where $I = \sqrt{-1}$. Experimentally, J_1 was extracted from differences in measurements of ellipsometric parameters Ψ and Δ of the oxide free, reduced surface at low electrode potentials, and measurements of surfaces with different degrees of oxidation. Furthermore, the data analysis processed in three steps. First, the dielectric function of the substrate was determined using the data from oxide-free potential region. Second, the thickness of the layer for each potential was calculated with two different approaches. Here, the first approach uses the shift in Δ with increase in the thickness of the layer [35]. The second approach assumes the oxide layer is non-absorbing at wavelengths >650 nm, and is otherwise a parameter-free analysis [32]. Up to potentials of +0.5 V, results from both approaches agree well. At higher potentials, the second approach sometimes shows numerical instabilities. Therefore, in this work the results of the second approach are shown only for the CV data. For CA experiments, results with the first approach only are shown here, because this method is independent of numerical problems. Finally, using the substrate dielectric function and layer thickness, the spectrum of the layer was obtained [31].

The advantage of using spectroscopic ellipsometry over using simple reflectance spectroscopy is that by using an ellipsometric detection scheme, one is less sensitive to morphology or roughness changes, in a situation analogous to the one described for incoherent scattering in ellipsometric scattering [36, 37]. In particular, the signal is unaffected by bubble formation up to a certain level, as shown previously when approaching hydrogen evolution [38].

2.3. Raman and photoluminescence (PL) spectroscopy

Both in situ and ex situ Raman spectroscopy measurements were conducted using a Labram confocal Raman microscope (Horiba Jobin Yvon, France). An objective with

magnification 10×, numerical aperture 0.25, was used to illuminate the sample with light from the 632 nm (1.96 eV) line of a HeNe laser for in situ experiments. Spectra were acquired for 10 s. For ex situ experiments, in addition to the 632 nm laser, light from the 514 nm (2.41 eV) line of an Ar^+ laser was also used.

Electrochemical experiments closely followed the conditions and protocols described in section 2.2. A specially built Teflon cell was used for electrochemical studies and in situ Raman spectroscopy [39]. A graphite rod was used as a counter electrode.

The same potential sequence was used as in ellipsometric experiments, however, the samples were polarised for different times at each potential, without finding a dependence on the hold time at the different potentials. Spectra recorded with a hold time of 10 min at each potential are shown here.

2.4. XPS

After in situ spectroscopic ellipsometry experiments, XPS (Quantera II, Physical Electronics, Chanhassen, MN, USA) was performed to investigate the chemical composition of the surface. The monochromatic Al Kα X-ray source (1486.6 eV) illuminated the sample surface. Photoelectrons were collected at a pass energy of 55 eV and a step size of 0.1 eV. The take-off angle was 45°. The binding energy scale was referenced to the C-C signal at 284.8 eV. Quantitative analysis was carried out with CasaXPS (http://www.casaxps.com/). Depth profiles were obtained by sputtering with an argon plasma at a voltage of 1 kV with a current of 2 mA to the target for the sputter steps. The sputtering rate under these conditions in copper was determined by sputtering through 27 nm evaporated copper on a silicon wafer as 2.87 nm min^{-1}.

2.5. Conductivity measurements

Classical Hall effect measurements in the van der Pauw configuration were performed to determine the mobility and type (n or p) of charge carriers at room temperature. Four Al contacts were bonded to the surface of a dry sample by ultrasonic wedge-bonding of 25 µm diameter Al wires at the 4 corners close to the circumference of the sample to measure the conductivity and Hall voltage of the surface layer [40–42]. For these experiments, samples were transferred through air atmosphere.

3. Results and discussion

3.1. Thickness of oxide during OER

First, the layer thickness of the oxide layer was extracted from ellipsometric data. Fig. 1 shows CV of Cu in 0.1M NaOH, which initially exhibited two cathodic features, C_2 and C_1, indicating the reduction of previously formed oxides on the surface [43, 44]. During a subsequent positive scan, two anodic peaks, A_1 and A_2, were observed.[2] These two peaks have been attributed to the formation of Cu^{I} and Cu^{II} oxides [43, 44]. The thickness of the oxide layer increased from its initial value by 2 nm with the first oxidation peak denoted as A_{1a} at -0.1 V. During the cathodic scan, the oxide on the surface was reduced in the potential region where reduction peaks (C_1 and C_2) were observed. In the anodic scan, the layer thickness continuously increased up to 14 nm due to oxidation of copper in the potential region where the oxidation peaks A_1 and A_2 were observed. Upon further potential increase between 0.1 and 0.8 V, minor changes in the oxide thickness were observed. The slight decrease in the oxide thickness during OER ($\approx$0.5 - 0.8 V) indicates that a dissolution of the oxide layer occurs upon entering the transpassive regime. Thermodynamically, OER is possible above 0.25 V [45].

Since the separation of time-dependent and potential-dependent features is not always possible in a CV scan [32], the nature of the oxide on Cu in the transpassive regime was investigated by potential step experiments (Fig. 2). Such experiments provide a more precise distinction between time and potential dependent processes. Similar to the CV experiments, 3 SE measurements were recorded at OCP before polarising the surface.

As shown in Fig. 2, a 4 nm thick initial oxide on the surface was initially reduced. In the positive scan, d jumped to 2 nm at -0.1 V and increased steadily to 10 nm until 0.9 V. However, d rapidly decreased during polarisation at a potential of 1.0 V. After reversing the scan direction at 1.0 V, d initially continued to decrease and reached a steady value around 0.8 V. After a final reduction step to -1.0 V, the resulting d was

[2] In line with common usage in the literature, different but similar notation is used to describe on the one hand peaks in the CV, and on the other hand the symmetry of vibrational modes observed in Raman spectra.

still 2 nm above the initial value. At this potential, an apparent thickness value may be obtained e.g. as a result of surface roughening due to oxide formation and reduction, as well as dissolution. The overall magnitude of the roughening is, however, sufficiently small to exclude a qualitative difference in the interpretation of the data.

In CA and CV experiments, similar total thickness values were obtained. On the other hand, the growth rate and evolution of the oxide film were different. During potential step experiments, at sufficiently high electrode potential the oxide became unstable and dissolved. A slight thickness decrease was also observed under potentiodynamic polarisation, but its overall magnitude was significantly lower. Upon potential decrease after entering the transpassive regime once, opposite trends were observed in CA and CV experiments. Under dynamic polarisation in CV, the thickness increased back to the initial value. On the other hand, after continuous polarisation at potentials were OER occurred, no thickness increase was observed. Furthermore, the potential range was slightly different in potentiostatic and potentiodynamic experiments, to 0.8 V in CV and to 1 V in CA, which could affect the observed thickness values. For water splitting over extended periods of time, the data gathered during potentiostatic polarisation is more relevant.

Thickness values obtained here are higher than some data available in the literature [46], and actually in most STM works [43, 44], as for thicker layers, tunnelling is not possible [47]. On the other hand, there are reports of thicker oxide layers on the order of 10 nm in slightly alkaline or acidic buffers [48]. It must be pointed out here that the thickness values obtained with the difference approach by ellipsometry used in this work are affected by a number of factors. Roughening of the surface will increase the obtained thickness. Also, changes in the surface structure other than oxide formation between the measurement of the oxide free surface and the surface covered by oxide, e.g. ion adsorption, or change in solvation, will contribute to the thickness value. Thickness values will also be overestimated if the refractive index of the formed oxide layer is significantly lower than for the copper oxides used to calculate the calibration relation for parameter Δ [35]. Deposition of previously dissolved species may also contribute to the thickness values, as during mounting of the cell, a certain time passes during which the electrode potential at the samples is not controlled, and during which dissolution

may occur. However, as the electrolyte is rinsed during these experiments, deposition is not expected to be a major factor influencing the thickness.

3.2. Structure of the film during OER and transpassive dissolution probed by Raman spectroscopy

To understand the structural evolution of the oxides during OER and transpassive dissolution, in situ Raman spectroscopy was conducted (Fig. 3 and Fig. 4).

The CV of Cu (Fig. 4a) measured during in situ Raman spectra acquisition agrees well with those obtained during in situ spectroscopic ellipsometry experiments, and those published in the literature [43, 44]. The in situ Raman spectrum of a Cu surface at OCP mainly showed the water deformation mode at ≈1640 cm^{-1}. While the ellipsometry and electrochemical data confirm the presence of a native oxide, this oxide may be to disordered to yield strong Raman peaks. Table 1 lists the Raman peaks observed in this work, together with possible assignments based on literature data of CuO, Cu_4O_3, Cu_2O and $Cu(OH)_2$ [30, 49–52].

Table 1: Raman peaks observed in this work with possible assignments [30, 49–52]. Reported peak wavenumbers in the literature vary considerably

Peak / cm^{-1}	System	Mode	Lit. peak / cm^{-1}
200	Cu_2O	$2E_u$	220
275	CuO	A_g	290
350	CuO	B_g	340
400	Cu_2O	multiphonon	400-490
480-490	Cu_2O	multiphonon	400-490
490	$Cu(OH)_2$	?	490
500	Cu_4O_3	E_g	505
530-540	Cu_4O_3	A_{1g}	540
560-570	?		
640	CuO	B_g	630-634
	Cu_4O_3	B_{1g}	630
	Cu_2O	T_{1u}	635

During the primary anodic A_{1a} peak (Fig. 4 b, -100 mV), a new characteristic spectral feature of Cu_4O_3 developed around 500 cm^{-1}, and dominated the spectra subsequently. A minor feature around 200 cm^{-1} indicated the presence of Cu_2O. These features indicate newly growing oxide at the interface. The Raman spectrum after complete reduction has similarities to the spectrum during the A_{1a} peak, but exhibits much lower peak intensities. This observation indicates that the oxide cannot be completely reduced in the experiments here, and that there must be areas at the surface which are not electrochemically accessible. A Raman spectrum of the surface recorded in the potential range of the A_1 peak is shown in Fig. 4b (-300 mV). Here, the presence of peaks at 190 and 638 cm^{-1} is attributed to the $2E_u$ and T_{1u} vibrational modes of Cu_2O. These observations are consistent with the formation Cu_2O with the first oxidation peak A_1. The feature at 500 cm^{-1} also shows the presence of Cu_4O_3. The spectrum recorded during the A_2 peak (Fig. 4) is still dominated by Cu_4O_3 features, with Cu_2O contributions at 190 cm^{-1}. Starting in the passive region (Fig. 4b, 0.4 V), the Cu_2O features disappear, and a feature at 275 cm^{-1}, indicating CuO formation, appeared. The CuO feature grew in intensity with increasing electrode potential (Fig. 4b, 0.6 V and above).

Upon entering the potential region where current increases and OER occurs, the Raman spectra change significantly (Fig. 4b, 0.8 V). Now, the intensity of the Cu_4O_3 feature which dominated the spectra so far decreased, and at the highest potentials, it was absent (Fig. 3b). The CuO feature remained, however, it did not become more prominent in the spectra (Fig. 3c). Moreover, photoluminescence was observed, as will be shown in more detail below (Fig. 5 - Fig. 7; measured during CA experiments). The PL peaked at $\approx$1.55 eV, with an asymmetric peak shape that has higher intensities at higher photon energies (Fig. 5). From all copper oxides, PL is typically only observed in Cu_2O [30]. In Cu_2O, PL around 1.5 eV was attributed to the presence of single charged oxygen vacancies, V_O^+, [3] [30]. However, more complex interpretations are possible.

The decrease in the intensity of the Cu_4O_3 peak correlates with the decrease in the thickness of oxide layer observed at the beginning of OER by in situ SE (Fig. 1). However, during ongoing transpassive dissolution, only slight changes in the thickness

[3] See [53] for a comment on the notation used.

were observed by SE. Together with in situ SE experiment, the Raman results indicate a sudden change in the oxidation state of a fraction of atoms in the oxide during OER, accompanied by a minor change in the oxide thickness. An important observation is that the Cu_4O_3 peak disappeared only after the current density already started to increase, i.e. during and not before transpassive dissolution set in.

Fig. 5 shows PL and Fig. 6 and 7 show Raman spectra recorded during CA experiments on copper foil. Generally, spectral features were much wider on Cu foil compared to evaporated Cu. This observation is attributed to the strong texturing of evaporated copper, which implies that evaporated Cu surfaces have a preferential surface orientation, as opposed to polycrystalline Cu foil. Dominating feature in the Raman spectra were also the Cu_4O_3 features around 500-550 cm^{-1}. Significant intensities were also observed between 450 and 500 cm^{-1}. Such features have in the past been observed in $Cu(OH)_2$ [50], but also been assigned to multiphonon processes in Cu_2O [30]. It remains therefore unclear how to interpret these features in the context of this work.

The comparison between Raman intensities and current density (Fig. 6) shows that the current increase, which started at 0.6 V, is not directly correlated to changes in the spectrum. The same observation was already made in CV experiments. Only at larger potentials, here around 1 V, the Raman peaks disappear completely. This correlated with the observed significant decrease in layer thickness at the same potential (section 3.1).

The generation of PL (Fig. 5 and Fig. 6) at 1.55 eV started for the first time around 0.7 V, and became dominant at 1 V (see section 3.3). The PL spectra remained unchanged, with the exception of an increase in PL intensities. At 1.0 V, all oxide Raman peaks disappeared and the spectrum was dominated by strong PL.

Upon decreasing the potential, only the PL remained in the spectra until a potential of 0.5 V was reached (Fig. 6. At lower potentials, PL disappeared, and the same features as during increasing potential became prominent.

3.3. Characteristics of the electronic structure of the oxide in the transpassive regime

The observation of PL at 1.5 eV is a strong indication of generation of oxygen vacancies during OER [30]. Both during CV and CA experiments, the observed changes

indicate the presence of a highly defective oxide during OER and transpassive dissolution.

Complementary to the PL observation, a detailed analysis of the absorption spectra from the ellipsometric data of the oxide can yield more information about the electronic structure of the oxides in the transpassive regime. Fig. 8 shows the absorption coefficient k of the oxide layer under different electrochemical conditions.

The spectrum of the oxide in the passive regime was discussed previously [31]. In this work, only the spectrum in the potential range where Cu transits from the passive to the transpassive regime shall be discussed, on the basis of a recent review [30]. The shape of spectra obtained here is completely different than the shape of spectra of bulk copper oxides, which has been noted before [31, 54]. All spectra show a peak at 2.1 eV. The electronic absorption at 2.1 eV is attributed to the yellow transition from Cu_2O, which is the forbidden direct band to band transition. This appearance of the otherwise forbidden transition is attributed to the presence of defects which lead to a relaxation of the transition rules. Furthermore, a developed feature at 3.7 eV is observed during OER in the CV experiment (Fig. 8a). The strongest feature from Cu_4O_3 is expected to be observed at this energy [30]. This strong increase in the absorption at 3.7 eV is assigned to the increased formation of Cu_4O_3.

Fig. 8b shows results from different potentials of a CA experiment during stepwise potential increase. The absorption peak at 2.1 eV shifted to 2.0 eV and became broader with increasing electrode potential. Moreover, a new feature appeared at 2.7 eV, which is assigned to the indigo transition of Cu_2O [30]. In the potential region of +0.7 V to +0.8 V, similar to CV experiment an absorption peak at 3.7 eV emergeed, which is attributed to increased formation of Cu_4O_3. Simultaneous changes occur in the absorption spectra in the potential range between 0.8 V to 0.9 V. Firstly, the peak at 2.0 eV shifted back to 2.1 eV. Secondly, the absorption from Cu_4O_3 shifted to lower energies by 0.2 eV. These changes indicate a remodelling of the oxide, likely due to the transport of defects and material in the oxide layer.

It is also interesting to investigate the spectra during the stepwise decrease in potential in CA experiments (Fig. 8c and d). The peak at 3.5 eV from Cu_4O_3 decreased in absorption when the potential switched back to 0.9 V. The spectra in the range between

0.9 V and -0.1 V are qualitatively the same as in previous work [31], suggesting the repassivation of the surface.

3.4. State of the surface after OER and transpassive dissolution

The Raman/PL spectra after removal of the sample from electrolyte (Fig. 9a) show no PL at 1.55 eV, which was prominent at the end of the in situ measurements. Raman features of CuO were observed around 280 cm^{-1} (compare Table 1). The peak at 596 cm^{-1} may indicate the usually Raman-inactive A_u mode of Cu_4O_3. This mode may become Raman-active due to symmetry break from point defects. The spectrum obtained after an SE-CA experiment (Fig. 9b) is qualitatively different from the spectra obtained during the in situ measurements. In Fig. 9b, PL at ≈1.7 eV indicates slightly shifted luminescence, which may be caused by surface vacancies. In addition, in Fig. 9b the Raman peaks of Cu_4O_3 and Cu_2O are observed at ≈500 and 200 cm^{-1}, respectively (compare Table 1).

Two dominant features, PL at 2.1 eV and 2.4 eV, were observed when the sample was excited with a sufficiently high photon energy (Fig. 9c). Since there is no PL reported for CuO and Cu_4O_3 [30], the PL observed here is attributed to the presence of Cu_2O. PL at 2.1 eV and 2.4 eV are in good agreement with the absorption spectrum in Fig. 8. Here, PL at 2.4 eV is assigned to the blue exciton transitions from Cu_2O [30]. The presence of the forbidden yellow transition in the absorption spectra as measured during the in situ SE experiment (Fig. 8) is supported by the presence of PL at roughly the same photon energy of 2.1 eV. Moreover, the E_u vibrational mode of Cu_2O, as well as the A_g and B_g vibrational modes of CuO are visible in Fig. 9c.

Overall, Raman spectroscopy is not very well suited to quantify different components. A quantitative interpretation of the absorption spectra is hampered by the fact that the individual components of the spectra are not equivalent to the well-known absorption spectra of the copper oxides. To complement the spectroscopic data, the chemical composition of the layer after in situ SE was studied by XPS depth profile investigations (Fig. 10). The sample was transferred through air.

The Cu 2p and Cu LMM spectra after the CV experiment (Fig. 10a and b) clearly show the presence of Cu^{II}, as evidenced by the presence of the satellite peak in Cu 2p,

and the position of the Cu LMM peak [55–58]. After the first sputtering step, the satellite peak in the Cu 2p spectrum indicates Cu^{I}, which is further confirmed by the position of the Cu LMM peak [55–58]. After sputtering 15-20 nm of the layer, the oxide film is removed completely, as evidenced by the shifts of the Cu 2p and Cu LMM peaks in Fig. 10a and b. This thickness value of ≈15 nm is in agreement with the thickness obtained from the thickness analysis of the in situ SE data.

The surface spectrum of the layer from the CA experiment (Fig. 10c and d) shows a satellite peak in Cu 2p pointing towards the presence of Cu^{I}, which is further confirmed by the Cu LMM spectrum [55–58]. A single sputtering step of ≈3 nm results in the removal of the oxide layer, as evidenced by the shift in the Cu 2p and Cu LMM spectra. The obtained thickness is also in agreement with the thickness obtained from the analysis of the in situ SE spectra.

Hall-effect measurements of the samples after the in situ experiments showed a carrier density of $(-5 \pm 1) \cdot 10^{18}$ cm^{-3} and mobility of (9 ± 2) cm^2/Vs. Uncertainty estimates were obtained as standard deviations from subsequent measurements with different current injections from 1 mA to 10 mA. Standard deviations of individual resistance measurements were in the order of 0.01%. All samples, whether subjected to OER or emersed before entering the transpassive regime, exhibited n-type conductivity, which contradicts the literature data for bulk copper oxides. These are reported to be p-type semiconductors [2, 30, 59]. Also in in situ photoelectrochemical experiments, the forming oxide films grown for a certain time or formed by reduction have been shown to be p-type [47, 60, 61]. The opposite observed in this work may be explained by the existence of a defect rich film produced due to electrode polarisation directly at the Cu/oxide interface. If the total films become too thin, the defect rich film may dominate the overall behaviour. However, an effect of the underlying metal layer on the measurements, or of a post-treatment modification during sample transfer as used in this work, cannot be excluded. Furthermore, the different methods used in the different experiments may simply weigh different type of defects in a different way; as it is clear that the films here are defect-dominated, different observations may also originate from method-specific differences.

3.5. Model for transpassive dissolution

The last observation shall be the starting point for a discussion of the overall behaviour. Cu_2O is intrinsically a p-type semiconductor [2, 30, 62, 63]. Therefore, the oxide film forming on copper is in general also treated as p-type. However, conductivity measurements performed here show the opposite: the defect rich semiconductor films even have a different nature of the semiconductor compared to bulk substance. This observation explains why the optical absorption spectra here and observed before [31] on copper on passive material are so different from the bulk absorption spectra of the oxides. The materials are simply significantly different in their structure, and the results suggest that this difference is even larger than previously observed for thin oxides on zinc [64].

Overall, the oxide layers consists of three different oxides: Cu_2O, Cu_4O_3 and CuO. No direct evidence is found here for the presence of copper species in an oxidation state > 2. Cu^{III} shows a characteristic blue absorption [29], which was not observed here. On the other hand, the complicated absorption spectra may simply hide features from species with higher valency. It is clear, however, that such species do not dominate the thin film. In the passive range, the layer mainly consists of Cu_2O and Cu_4O_3 [31]. As opposed to the previous work [31], CuO was already found in the passive regime, likely because here, the system wasn't given sufficient time for relaxation an complete formation of the mixed oxide. However, it is still observed here that oxide growth steps do not agree with potential steps.

At the onset of the current increase, i.e. where OER and transpassive dissolution are supposed to occur, the spectral changes observed are initially limited. Only well into the transpassive regime, when the electrode potential reached 1.0 V, the total layer thickness decreased. At the same time, a defect related PL suddenly startd to dominate the spectra, an absorption feature of Cu_4O_3 became significantly stronger, while the Raman line of Cu_4O_3 broadened significantly. Therefore, Cu_4O_3 must play an important role in the OER. (In potentiodynamic experiments, Raman features of CuO become more prominent during the OER.) Dissolution and OER happen at the solution/oxide interface. It is likely that some of the O atoms consumed in the OER originate from within the oxide film, which is why oxygen vacancies are formed that lead to the ob-

served PL. At the same time, more Cu^{II} species are formed, which makes inner part of the film, Cu_2O, transform into Cu_4O_3 by partial oxidation of a fraction of copper ions. Increased generation of both cation and anion vacancies and subsequent vacancy pair coalescence is the main mechanism of transpassive film dissolution suggested by the point defect model [19]. Loss in thickness coinciding with defect generation is hence not unexpected.

The observed PL is not expected for a situation in which the Fermi level is within the valence band. In this situation, the spectrum should closely resemble the spectrum of a metal, where no PL occurs, and where the absorption suddenly increases significantly and has no distinct peaks but is essentially a curved line. On the other hand, it is possible that the PL originates from the inner part of the layer, where the Fermi level is still above the valence band, and only the surface behaves metal-like.

Recently, predominance diagrams of defects in semiconductors have been obtained from ab initio calculations of defect levels, for the example of ZnO [53, 65]. The experimental observations especially in the CA experiments suggest that above a certain potential, the Cu oxides become unstable with respect to defect formation, which results in the observed PL. According to all the current state of literature on bulk and thin film oxides [30], the observed PL should originate from Cu_2O. The different observed PL bands of Cu_2O are assigned to transitions induced by doubly charged oxygen vacancies (V_O^{2+}) at 1.72 eV/720 nm, singly charged oxygen vacancies (V_O^{+}) at 1.53 eV/810 nm, and copper vacancies (V_{Cu}) at 1.35 eV (920 nm) [30]. Following this classical interpretation of PL spectra [30], starting at 0.9 V, single charged oxygen vacancies V_O^{+} become the dominating stable species. It must be noted, however, that the observed energies do not exactly agree with those reported in the literature [30]. This slight disagreement may be a hint that other defects, or other lattices, could be involved. The p-type conductivity of bulk Cu_2O is caused by negatively charged Cu vacancies, V_{Cu}^{-}, whereas the positively charged oxygen vacancies V_O^{+} and V_O^{2+} form donor states [62, 63, 66]. The carrier polarity, density and mobility probed in the Hall effect measurement shows that the oxide obtained here has n-type conductivity. The PL spectra are dominated by an emission which also supports n-type conductivity. Hall effect measurements are dominated by the more mobile type of defects, while PL measurements are dominated by the

strongest emission. In Cu_2O, complex formation between V_O^+/V_O^{2+} and V_{Cu}^- has been shown [62]. In the defective thin oxide films, such a process is also likely to occur, so that the observations in this work do not rule out the presence of the typical V_{Cu}^- defects in the system. While ab initio data is not available yet for the involved copper oxides, it is likely that an instability towards defect formation is the reasons for the disintegration of the oxide layer above ≈0.9 V and the concurrent onset of strong defect-related PL.

The different behaviour during CV and CA experiment indicates that the time-dependent processes play an important role; this is not surprising, as the highly dynamic oxide during OER must undergo relaxation processes.

It is interesting to note that a strong increase in defect related luminescence in oxide-based conversion coatings was observed during cathodic polarisation [67]. In that case, however, almost no concurrent dissolution of the oxide was observed. The defects generated upon entering the transpassive regime observed in this work may therefore also be formed simply due to the charge transport and not necessarily by oxide consumption in OER.

Data gathered in this work is in part consistent with the point defect model [19], according to which cation vacancies at the surface move through the metal|oxide interface thus leading to the surface layer exhibiting n-type behaviour. While anion vacancies were observed by PL in this work, leading to the n-type behaviour of the surfaces as observed here, vacancy pairing [62] is likely to be present in the highly defective films. The mobile species may hence still be the cation vacancies, in line with a model for bulk Cu_2O [62]. On the other hand, the observed spectra are not consistent with the textbook picture of the Fermi level being pulled into the valence band, which leads to dissolution.

4. Conclusions

On copper, OER occured on an oxide covered surface, and transpassive dissolution also proceeded via a surface oxide. Like in the passive oxide, the mixed oxide Cu_4O_3 dominated the oxide film in the transpassive state. Upon transition to the transpassive state, Cu_4O_3 became strongly defective, as shown by the broadening of the Raman peak.

The oxide in the transpassive state is highly dynamic. The oxide film started disintegrating 0.3 V above the potential when the current was first observed to rise due to OER and transpassive dissolution: the layer thickness decreased to 10% of the maximum value, and defect-related PL was observed. Both phenomena were not directly linked to a jump in electrode potential. Defect formation was likely occurring in the inner region of the film, which is Cu_2O-like, and became unstable towards the formation of oxygen vacancies, V_O^+. The development of oxygen vacancies may be related to the consumption of oxygen through OER.

The oxide layers formed exhibited n-type semiconducting behaviour, in stark contrast to the expectation from the situation in bulk copper oxides.

What is clearly needed for water splitting to become widely used is a decoupling of OER and transpassive dissolution. The results from this work suggest that one needs to find a system where the oxide is stable towards defect formation up to electrode potentials sufficiently high to drive OER at industrially relevant current densities.

Acknowledgements

C.T. acknowledges the International Max Planck Research School for Surface and Interface Engineering in Advanced Materials (IMPRS SurMat) for a scholarship and Abdel Altin for helpful discussions on electrochemistry. Arne Ludwig and Nadine Viteritti are acknowledged for technical assistance with the Hall measurements. M. Stratmann is acknowledged for continuous support, and the MPIE workshop for building the in situ cells.

References

[1] H. Kaesche, Corrosion of Metals: Physicochemical Principles and Current Problems, Springer, Berlin, Germany, 2003.

[2] J. W. Schultze, A. W. Hassel, Encyclopedia of Electrochemistry, Vol. 4, Wiley-VCH, Weinheim, 2007, Ch. Passivity of Metals, Alloys and Semiconductors, pp. 216–235.

[3] H.-H. Strehblow, Passivity of metals studied by surface analytical methods, a review, Electrochim. Acta 212 (2016) 630 – 648. doi:10.1016/j.electacta.2016.06.170.

[4] L. D. Burke, A. Moynihan, Oxygen electrode reaction. Part 1.—Nature of the inhibition process, Trans. Faraday Soc. 67 (1971) 3550–3557. doi:10.1039/TF9716703550.

[5] L. D. Burke, O. J. Murphy, J. F. O'Neill, S. Venkatesan, The oxygen electrode. Part 8.—Oxygen evolution at ruthenium dioxide anodes, J. Chem. Soc., Faraday Trans. 1 73 (1977) 1659–1671. doi:10.1039/F19777301659.

[6] M. H. Miles, E. A. Klaus, B. P. Gunn, J. R. Locker, W. E. Serafin, S. Srinivasan, The oxygen evolution reaction on platinum, iridium, ruthenium and their alloys at 80°C in acid solutions, Electrochim. Acta 23 (1978) 521–526. doi:10.1016/0013-4686(78)85030-0.

[7] S. Gottesfeld, S. Srinivasan, Electrochemical and optical studies of thick oxide layers on iridium and their electrocatalytic activities for the oxygen evolution reaction, J. Electroanal. Chem. Interfacial Electrochem. 86 (1978) 89–104. doi:10.1016/S0022-0728(78)80358-1.

[8] M. S. Burke, L. J. Enman, A. S. Batchellor, S. Zou, S. W. Boettcher, Oxygen Evolution Reaction Electrocatalysis on Transition Metal Oxides and (Oxy)hydroxides: Activity Trends and Design Principles, Chem. Mater. 27 (2015) 7549–7558. doi:10.1021/acs.chemmater.5b03148.

[9] R. L. Doyle, M. E. G. Lyons, An electrochemical impedance study of the oxygen evolution reaction at hydrous iron oxide in base, Phys. Chem. Chem. Phys. 15 (2013) 5224–5237. doi:10.1039/C3CP43464H.

[10] Y. Matsumoto, E. Sato, Electrocatalytic properties of transition metal oxides for oxygen evolution reaction, Mater. Chem. Phys. 14 (1986) 397–426. doi:10.1016/0254-0584(86)90045-3.

[11] B. E. Conway, Electrochemical oxide film formation at noble metals as a surface-chemical process, Prog. Surf. Sci. 49 (1995) 331–452. doi:10.1016/0079-6816(95)00040-6.

[12] M. E. G. Lyons, R. L. Doyle, I. Godwin, M. O'Brien, L. Russell, Hydrous Nickel Oxide: Redox Switching and the Oxygen Evolution Reaction in Aqueous Alkaline Solution, J. Electrochem. Soc. 159 (2012) H932–H944. doi:10.1149/2.078212jes.

[13] A. C. C. Tseung, S. Jasem, Oxygen evolution on semiconducting oxides, Electrochim. Acta 22 (1977) 31–34. doi:10.1016/0013-4686(77)85049-4.

[14] H. G. Sanchez Casalongue, M. L. Ng, S. Kaya, D. Friebel, H. Ogasawara, A. Nilsson, In Situ Observation of Surface Species on Iridium Oxide Nanoparticles during the Oxygen Evolution Reaction, Angew. Chem. Int. Ed. 53 (2014) 7169–7172. doi:10.1002/anie.201402311.

[15] C. R. Clayton, Y. C. Lu, A bipolar model of the passivity of stainless steels—III. The mechanism of MoO_4^{2-} formation and incorporation, Corros. Sci. 29 (1989) 881–898. doi:10.1016/0010-938X(89)90059-0.

[16] Y. C. Lu, C. R. Clayton, A. R. Brooks, A bipolar model of the passivity of stainless steels—II. The influence of aqueous molybdate, Corros. Sci. 29 (1989) 863–880. doi:10.1016/0010-938X(89)90058-9.

[17] M. Bojinov, I. Betova, G. Fabricius, T. Laitinen, R. Raicheff, T. Saario, The stability of the passive state of iron–chromium alloys in sulphuric acid solution, Corros. Sci. 41 (1999) 1557–1584. doi:10.1016/S0010-938X(99)00003-7.

[18] A. Fattah-alhosseini, A. Saatchi, M. A. Golozar, K. Raeissi, The transpassive dissolution mechanism of 316L stainless steel, Electrochim. Acta 54 (2009) 3645–3650. doi:10.1016/j.electacta.2009.01.040.

[19] D. D. Macdonald, The history of the point defect model for the passive state: A brief review of film growth aspects, Electrochim. Acta 56 (2011) 1761 – 1772. doi:10.1016/j.electacta.2010.11.005.

[20] E. Sikora, D. D. Macdonald, Nature of the passive film on nickel, Electrochim. Acta 48 (2002) 69 – 77. doi:10.1016/S0013-4686(02)00552-2.

[21] A. I. Nguyen, M. S. Ziegler, P. Oña-Burgos, M. Sturzbecher-Hohne, W. Kim, D. E. Bellone, T. D. Tilley, Mechanistic Investigations of Water Oxidation by a Molecular Cobalt Oxide Analogue: Evidence for a Highly Oxidized Intermediate and Exclusive Terminal Oxo Participation, J. Am. Chem. Soc. 137 (2015) 12865–12872. doi:10.1021/jacs.5b08396.

[22] M. Huynh, C. Shi, S. J. L. Billinge, D. G. Nocera, Nature of Activated Manganese Oxide for Oxygen Evolution, J. Am. Chem. Soc. 137 (2015) 14887–14904. doi:10.1021/jacs.5b06382.

[23] K. S. Joya, X. Sala, In situ Raman and surface-enhanced Raman spectroscopy on working electrodes: spectroelectrochemical characterization of water oxidation electrocatalysts, Phys. Chem. Chem. Phys. 17 (2015) 21094–21103. doi:10.1039/C4CP05053C.

[24] M. W. Louie, A. T. Bell, An Investigation of Thin-Film Ni–Fe Oxide Catalysts for the Electrochemical Evolution of Oxygen, J. Am. Chem. Soc. 135 (2013) 12329–12337. doi:10.1021/ja405351s.

[25] B. J. Trześniewski, O. Diaz-Morales, D. A. Vermaas, A. Longo, W. Bras, M. T. Koper, W. A. Smith, In Situ Observation of Active Oxygen Species in Fe-Containing Ni-Based Oxygen Evolution Catalysts: The Effect of pH on Electrochemical Activity, J. Am. Chem. Soc. 137 (2015) 15112–15121. doi:10.1021/jacs.5b06814.

[26] B. S. Yeo, A. T. Bell, In Situ Raman Study of Nickel Oxide and Gold-Supported Nickel Oxide Catalysts for the Electrochemical Evolution of Oxygen, J. Phys. Chem. C 116 (2012) 8394–8400. doi:10.1021/jp3007415.

[27] D. Wang, J. Zhou, Y. Hu, J. Yang, N. Han, Y. Li, T.-K. Sham, In Situ X-ray Absorption Near-Edge Structure Study of Advanced $NiFe(OH)_x$ Electrocatalyst

on Carbon Paper for Water Oxidation, J. Phys. Chem. C 119 (2015) 19573–19583. doi:10.1021/acs.jpcc.5b02685.

[28] B. S. Yeo, A. T. Bell, Enhanced Activity of Gold-Supported Cobalt Oxide for the Electrochemical Evolution of Oxygen, J. Am. Chem. Soc. 133 (2011) 5587–5593. doi:10.1021/ja200559j.

[29] N. Wiberg, Hollemann-Wiberg - Lehrbuch der Anorganischen Chemie, 101st edition, Walter de Gruyter, Berlin, 1995, p. 1194.

[30] B. K. Meyer, A. Polity, D. Reppin, M. Becker, P. Hering, P. J. Klar, T. Sander, C. Reindl, J. Benz, M. Eickhoff, C. Heiliger, M. Heinemann, J. Bläsing, A. Krost, S. Shokovets, C. Müller, C. Ronning, Binary copper oxide semiconductors: From materials towards devices, Phys. Status Solidi B 249 (2012) 1487–1509. doi:10.1002/pssb.201248128.

[31] C. Toparli, A. Sarfraz, A. Erbe, A new look at oxide formation at the copper/electrolyte interface by in situ spectroscopies, Phys. Chem. Chem. Phys. 17 (2015) 31670–31679. doi:10.1039/C5CP05172J.

[32] Y. Chen, A. Erbe, In situ spectroscopic ellipsometry during electrochemical treatment of zinc in alkaline carbonate electrolyte, Surf. Sci. 607 (2013) 39–46. doi:10.1016/j.susc.2012.08.006.

[33] Y. Chen, P. Schneider, A. Erbe, Investigation of native oxide growth on zinc in different atmospheres by spectroscopic ellipsometry, Phys. Status Solidi A 209 (2012) 846–853. doi:10.1002/pssa.201100542.

[34] J. Lekner, Theory of Reflection of Electromagnetic and Particle Waves, Martinus Nijhoff, Dordrecht, The Netherlands, 1987.

[35] Role of copper oxides in contact killing of bacteria, Langmuir 29 (2013) 16160–16166. doi:10.1021/la404091z.

[36] R. Sigel, A. Erbe, Effects of sample polydispersity and beam profile on ellipsometric light scattering, Appl. Opt. 47 (2008) 2161–2170. doi:10.1364/AO.47.002161.

[37] A. Erbe, K. Tauer, R. Sigel, Separation of coherent and incoherent scattering contributions in ellipsometric light scattering experiments on latex mixtures, Langmuir 25 (2009) 2703–2710. doi:10.1021/la803500p.

[38] N. Kemnade, Y. Chen, M. I. Muglali, A. Erbe, Electrochemical reductive desorption of alkyl self-assembled monolayers studied in situ by spectroscopic ellipsometry: evidence for formation of a low refractive index region after desorption, Phys. Chem. Chem. Phys. 16 (2014) 17081–17090. doi:10.1039/C4CP01369G.

[39] G. Genchev, A. Erbe, Raman spectroscopy of mackinawite FeS in anodic iron sulfide corrosion products, J. Electrochem. Soc. 163 (2016) C333–C338. doi:10.1149/2.1151606jes.

[40] L. van der Pauw, A method of measuring the resistivity and Hall coefficient on lamellae of arbitrary shape, Philips Tech. Rev. 20 (1958/59) 220–224.

[41] A. Ramadan, R. Gould, A. Ashour, On the Van der Pauw method of resistivity measurements, Thin Solid Films 239 (1994) 272 – 275. doi:10.1016/0040-6090(94)90863-X.

[42] D. K. de Vries, A. D. Wieck, Potential distribution in the van der Pauw technique, Am. J. Phys. 63 (1995) 1074–1078. doi:10.1119/1.18013.

[43] V. Maurice, H. H. Strehblow, P. Marcus, In situ STM study of the initial stages of oxidation of Cu(111) in aqueous solution, Surf. Sci. 458 (2000) 185–194. doi:10.1016/S0039-6028(00)00442-8.

[44] J. Kunze, V. Maurice, L. H. Klein, H.-H. Strehblow, P. Marcus, In situ STM study of the effect of chlorides on the initial stages of anodic oxidation of Cu(111) in alkaline solutions, Electrochim. Acta 48 (2003) 1157–1167. doi:10.1016/S0013-4686(02)00826-5.

[45] P. Vanýsek, CRC Handbook of Chemistry and Physics, 93rd Edition (Internet Version 2013), CRC Press/Taylor and Francis, Boca Raton, FL, 2013, Ch. Electrochemical Series, pp. 5–80 – 5–89.

[46] H. D. Speckmann, S. Haupt, H.-H. Strehblow, A quantitative surface analytical study of electrochemically-formed copper oxides by XPS and X-ray-induced Auger spectroscopy, Surf. Interface Anal. 11 (1988) 148–155. doi:10.1002/sia.740110305.

[47] H.-H. Strehblow, V. Maurice, P. Marcus, Initial and later stages of anodic oxide formation on Cu, chemical aspects, structure and electronic properties, Electrochim. Acta 46 (2001) 3755 – 3766. doi:10.1016/S0013-4686(01)00657-0.

[48] H.-H. Strehblow, B. Titze, The investigation of the passive behaviour of copper in weakly acid and alkaline solutions and the examination of the passive film by ESCA and ISS, Electrochim. Acta 25 (1980) 839 – 850. doi:10.1016/0013-4686(80)90036-5.

[49] H. Y. H. Chan, C. G. Takoudis, M. J. Weaver, Oxide Film Formation and Oxygen Adsorption on Copper in Aqueous Media As Probed by Surface-Enhanced Raman Spectroscopy, J. Phys. Chem. B 103 (1999) 357–365. doi:10.1021/jp983787c.

[50] J. C. Hamilton, J. C. Farmer, R. J. Anderson, In Situ Raman Spectroscopy of Anodic Films Formed on Copper and Silver in Sodium Hydroxide Solution, J. Electrochem. Soc. 133 (1986) 739–745. doi:10.1149/1.2108666.

[51] L. Debbichi, M. C. Marco de Lucas, J. F. Pierson, P. Krüger, Vibrational Properties of CuO and Cu_4O_3 from First-Principles Calculations, and Raman and Infrared Spectroscopy, J. Phys. Chem. C 116 (2012) 10232–10237. doi:10.1021/jp303096m.

[52] Z. Jiang, S. Tian, S. Lai, R. D. McAuliffe, S. P. Rogers, M. Shim, D. P. Shoemaker, Capturing phase evolution during solvothermal synthesis of metastable Cu_4O_3, Chem. Mater. 28 (2016) 3080–3089. doi:10.1021/acs.chemmater.6b00421.

[53] M. Todorova, J. Neugebauer, Identification of bulk oxide defects in an electrochemical environment, Faraday Discuss. 180 (2015) 97–112. doi:10.1039/C4FD00238E.

[54] H.-H. Strehblow, H.-D. Speckmann, Corrosion and layer formation of passive copper in alkaline solutions, Mater. Corros. 35 (1984) 512–519. doi:10.1002/maco.19840351104.

[55] T. Fleisch, G. Mains, Reduction of copper oxides by UV radiation and atomic hydrogen studied by XPS, Appl. Surf. Sci. 10 (1982) 51 – 62. doi:10.1016/0378-5963(82)90134-9.

[56] G. Panzner, B. Egert, H. Schmidt, The stability of CuO and Cu_2O surfaces during argon sputtering studied by XPS and AES, Surf. Sci. 151 (1985) 400 – 408. doi:10.1016/0039-6028(85)90383-8.

[57] K. J. Blobaum, D. Van Heerden, A. J. Wagner, D. H. Fairbrother, T. P. Weihs, Sputter-deposition and characterization of paramelaconite, J. Mater. Res. 18 (2003) 1535–1542. doi:10.1557/JMR.2003.0212.

[58] R. Benoit, Y. Durand, B. Narjoux, G. Quintana, http://www.lasurface.com/ (October 2016).

[59] Y. S. Lee, M. T. Winkler, S. C. Siah, R. Brandt, T. Buonassisi, Hall mobility of cuprous oxide thin films deposited by reactive direct-current magnetron sputtering, Appl. Phys. Lett. 98 (2011) 192115. doi:10.1063/1.3589810.

[60] U. Collisi, H.-H. Strehblow, A photoelectrochemical study of passive copper in alkaline solutions, J. Electroanal. Chem. Interfacial Electrochem. 210 (1986) 213 – 227. doi:10.1016/0022-0728(86)80573-3.

[61] U. Collisi, H.-H. Strehblow, The formation of Cu_2O layers on Cu and their electrochemical and photoelectrochemical properties, J. Electroanal. Chem. Interfacial Electrochem. 284 (1990) 385 – 401. doi:10.1016/0022-0728(90)85046-8.

[62] A. Mittiga, F. Biccari, C. Malerba, Intrinsic defects and metastability effects in Cu_2O, Thin Solid Films 517 (2009) 2469 – 2472. doi:10.1016/j.tsf.2008.11.054.

[63] M. Nolan, S. D. Elliott, Tuning the electronic structure of the transparent conducting oxide Cu_2O, Thin Solid Films 516 (2008) 1468 – 1472. doi:10.1016/j.tsf.2007.03.073.

[64] Y. Chen, P. Schneider, B.-J. Liu, S. Borodin, B. Ren, A. Erbe, Electronic structure and morphology of dark oxides on zinc generated by electrochemical treatment, Phys. Chem. Chem. Phys. 15 (2013) 9812–9822. doi:10.1039/C3CP44714F.

[65] M. Todorova, J. Neugebauer, Extending the concept of defect chemistry from semiconductor physics to electrochemistry, Phys. Rev. Appl. 1 (2014) 014001. doi:10.1103/PhysRevApplied.1.014001.

[66] M. Nolan, Defects in Cu_2O, $CuAlO_2$ and $SrCu_2O_2$ transparent conducting oxides, Thin Solid Films 516 (2008) 8130 – 8135. doi:10.1016/j.tsf.2008.04.020.

[67] A. Sarfraz, R. Posner, A. Bashir, A. Topalov, K. J. J. Mayrhofer, K. Lill, A. Erbe, Effect of polarisation mimicking cathodic electrodeposition coating on industrially relevant metal substrates with ZrO_2-based conversion coatings, ChemElectroChem 3 (2016) 1415–1421. doi:10.1002/celc.201600216.

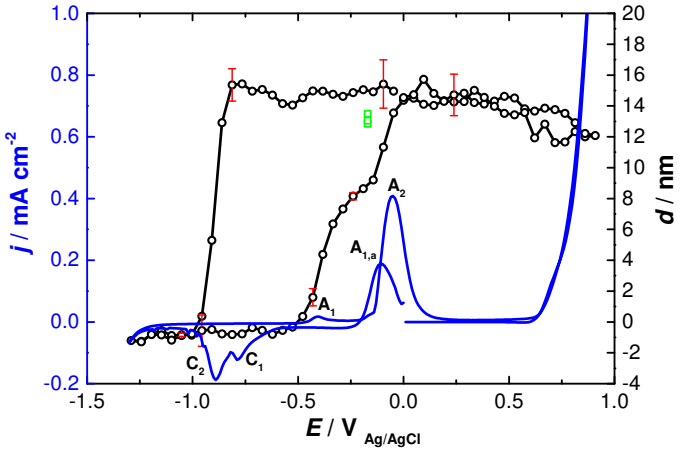

Figure 1: First scan of CV between -1.3 V and 0.8 V vs. Ag|AgCl|3M KCl started at 0 V on a surface covered with previously formed oxide. The current density j (—) and layer thickness d (∘) are plotted against potential E. Values for d were obtained using a parameter free analysis method [32]. The scan rate was 2 mV s^{-1}, thus each SE spectrum averages over 47 mV. The first three SE measurements (□) were recorded at open circuit potential (OCP), ≈-170 mV. Representative uncertainty estimates (⌶) are shown only on selected thickness points to keep the graph legible.

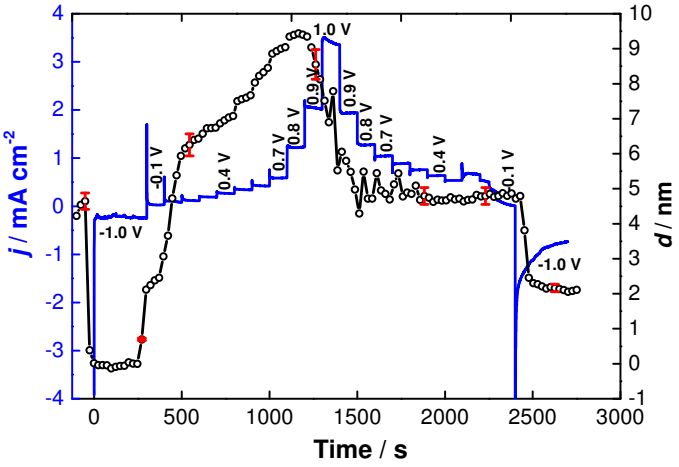

Figure 2: Current density j (—) and thickness d (∘) of oxide layer as a function of time at certain applied electrode potentials, which are in part indicated in the graph (see section 2.2). Layer thickness shown was obtained by an analysis of the shift in ellipsometric parameter Δ [35]. Representative uncertainty estimates (⌶) are only shown on selected thickness points to keep the graph legible.

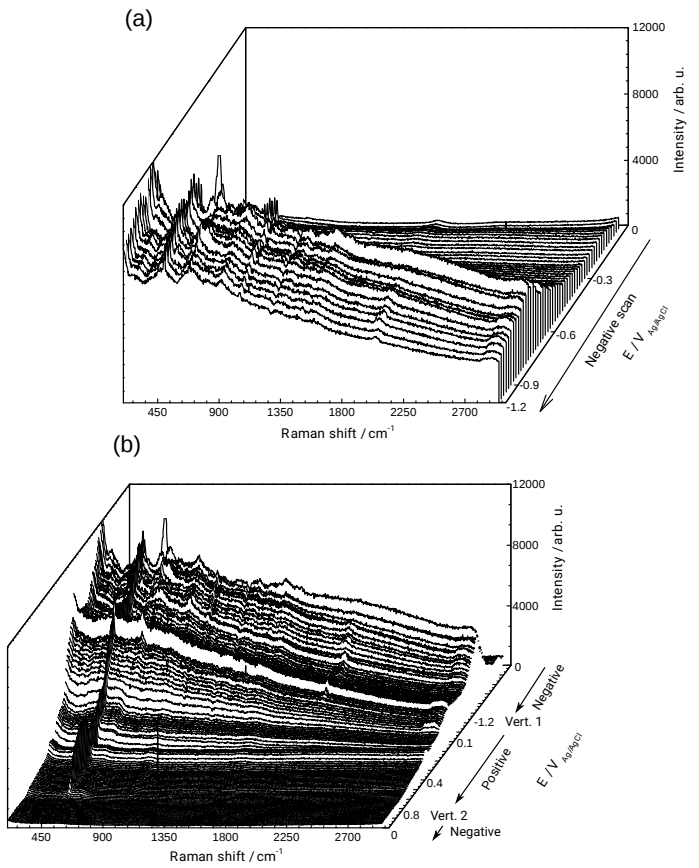

Figure 3: Evolution of in situ Raman spectra (excitation: 633 nm / 1.96 eV) collected during a CV with scan rate 2 mV s^{-1} in the potential range from -1.2 V to 0.8 V. Selected spectra are shown enlarged in Fig. 4. (a) Initial phase of the experiment, from start to negative vertex at -1.2 V. (b) Full potential range, starting from 0 V (back), proceeding to the negative vertex potential of -1.2 V (Vert. 1), then to the positive vertex potential of 0.8 V (Vert. 2), and back to the potential of 0 V (front). "Positive" and "negative" indicate the scanning direction in the particular phase of the experiment.

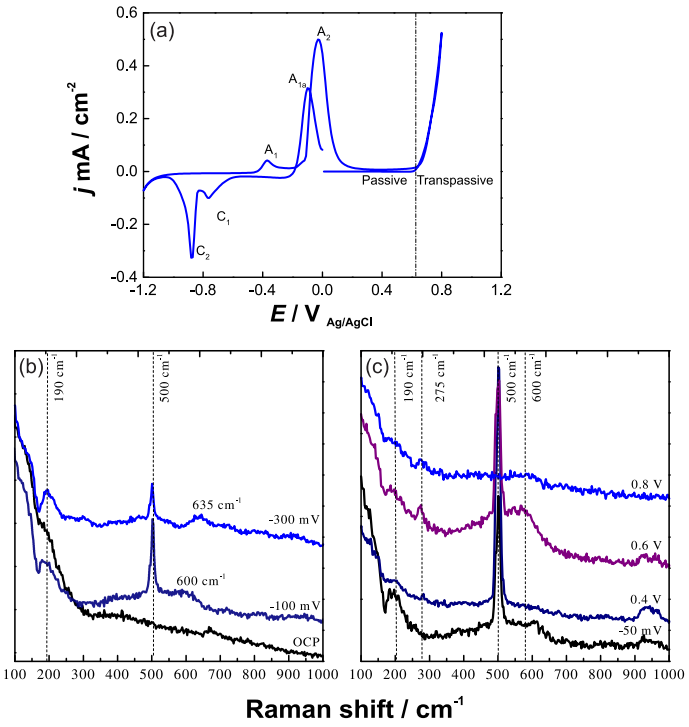

Figure 4: Examples of in situ Raman spectra (excitation: 633 nm / 1.96 eV) collected during (a) CV (2 mV s^{-1}) of evaporated Cu at selected, representative potentials as indicated in the graph, in the potential range of -1.2 V and 0.8 V, in 0.1M NaOH. The full series is shown in Fig. 3; (b) during initial phase, at OCP, initial peak A_{1a} (-0.1 V) and first oxidation peak A_1 (0.3 mV); (c) second oxidation peak A_2 (-0.05 V), passive region (0.4 V) at onset of OER and at running OER (0.8 V)

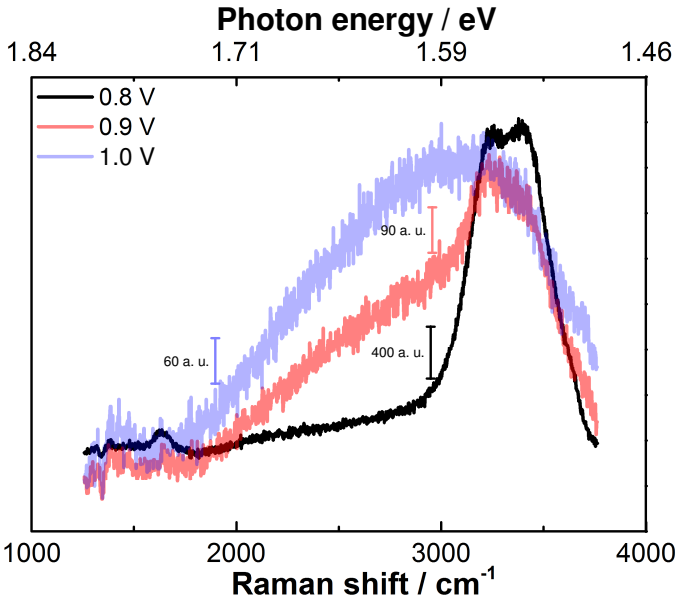

Figure 5: Representative Raman and PL spectra (excitation: 633 nm / 1.96 eV) recorded in situ during CA experiments at 0.8 V, 0.9 V and 1.0 V, with an extended spectral range compared to the spectra shown in Fig. 6 and Fig. 7. The numbers on the photon energy scale correspond in the closest third digit to the energy value of the wavelength at which the respective Raman shift was detected.

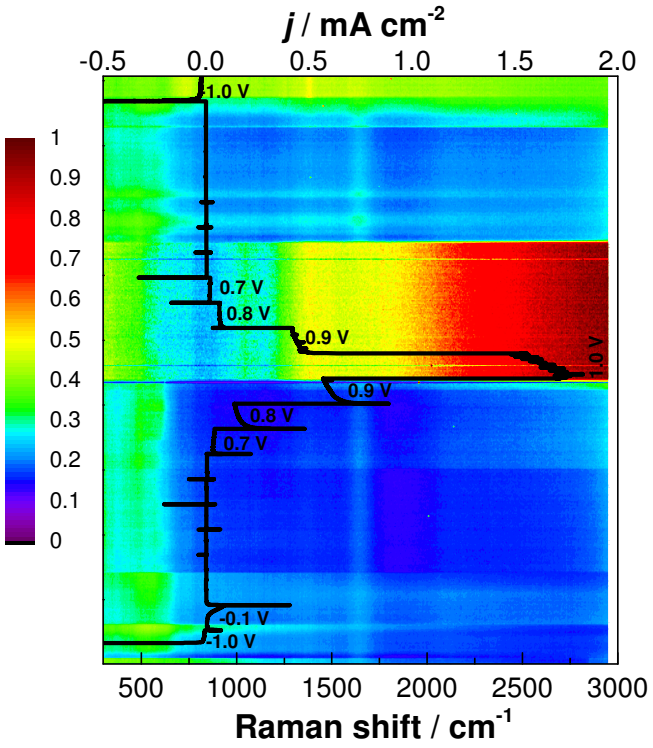

Figure 6: Colour-coded Raman and PL spectra (excitation: 633 nm / 1.96 eV) recorded during CA experiments, superimposed with current density data. The ordinate axis presents the progress of the experiment. Recorded current densities are displayed with the top axis as current density axis. Selected applied potentials are indicated in the graph. The bottom axis is the wavenumber axis for the false coloured Raman spectra. Spectra have been normalised by the maximum intensity recorded in the series. The intensity colour scale is shown on the left. Representative spectra at selected potentials are shown in Fig. 7.

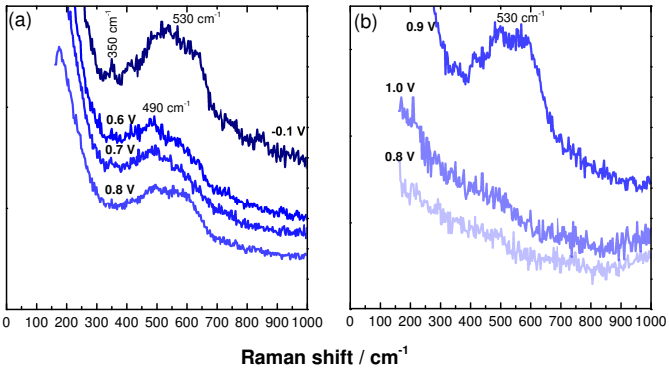

Figure 7: Potential dependent in situ Raman spectra (excitation: 633 nm / 1.96 eV) acquired during CA experiments at the potentials as indicated in the graph. Current data is shown in Fig. 6. (a) shows spectra during increasing potential up to 0.8 V; (b) shows spectra during running OER at 0.9 V, at 1.0 V and the spectrum after stepping back in negative direction to 0.8 V.

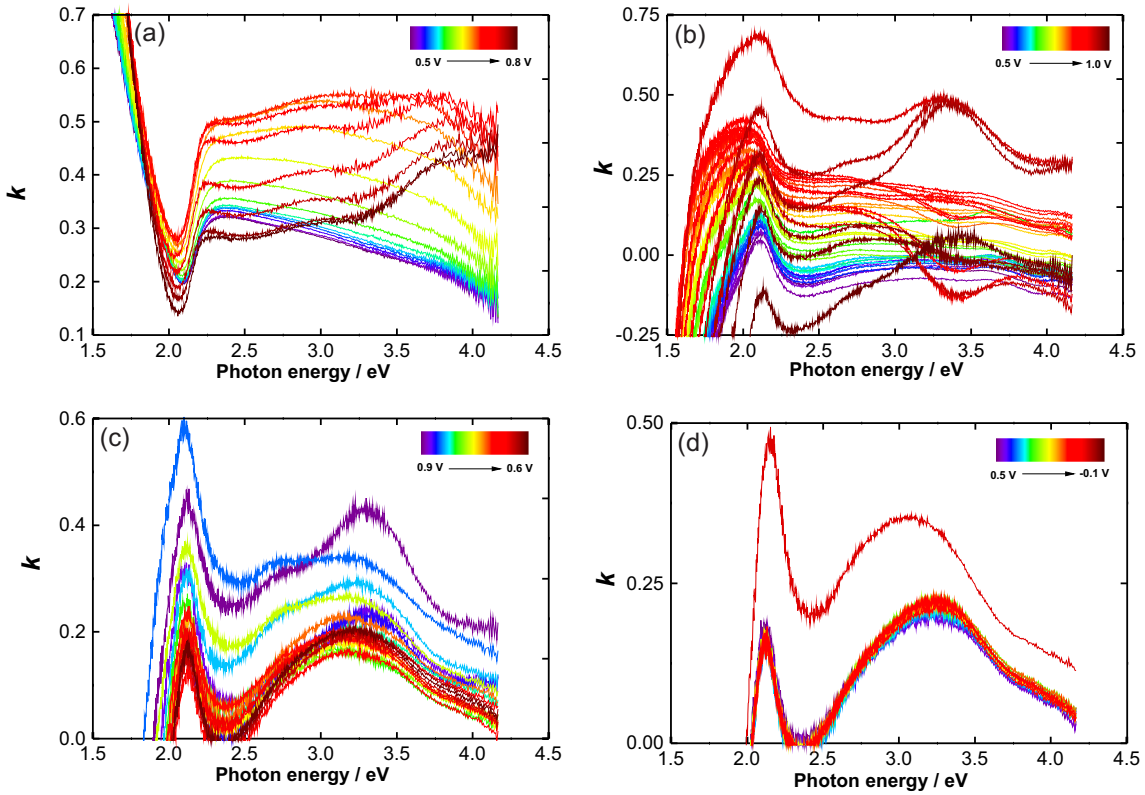

Figure 8: Imaginary part *k* of refractive index of the oxide layer on copper obtained in situ (a) during a CV experiment in the potential range 0.5 V to 0.8 V. Same quantity from CA experiments in the potential range (b) 0.5 V to 1.0 V (increasing potential), (c) 0.9 to 0.6 V (decreasing potential), and (d) 0.5 to -0.1 V (decreasing potential).

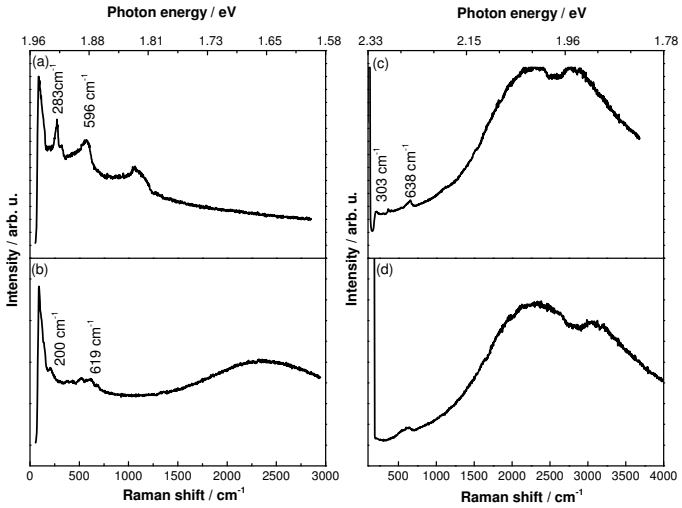

Figure 9: Raman/PL spectra recorded ex situ, excited with 633 nm/1.96 eV (a) after a one cycle SE-CV experiment terminated at 0 V, and (b) after a full cycle SE-CA experiment terminated at -1.0 V. Spectra with 514 nm/2.41 eV excitation (c) after SE-CV experiment (d) after SE-CA experiment, both after the same treatment as (a) and (b).

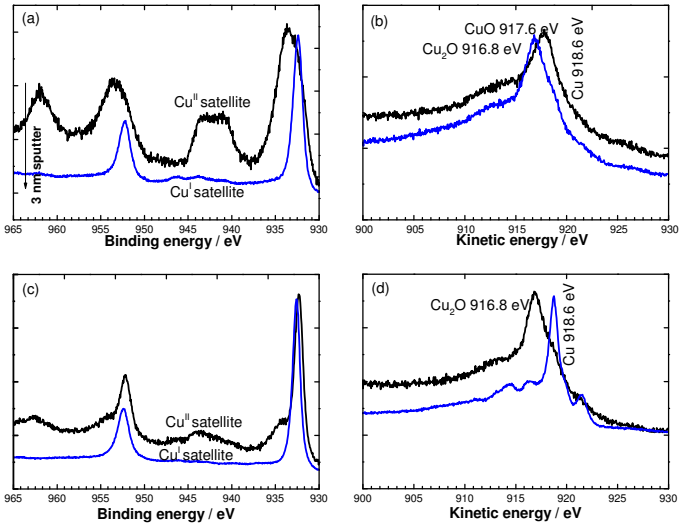

Figure 10: Analysis of the surface after CV experiment, (a) Cu 2p XP spectra and (b) Auger LMM spectra. Surface after CA experiment, (c) Cu 2p XP spectra and (d) Auger LMM spectra. — surface; — after 3 nm sputtering.